Stability Prediction of Integrated-Circuit Based Constant ON-Time Controlled Buck Converters

Brian Wang, Dan Chen, *Fellow, IEEE*, Ching-Jan Chen, *Senior Member, IEEE*, and Sheng-Fu Hsiao

***Abstract*—The commonly used average model is not applicable to predict the stability performances of constant ON-time (COT) controlled buck converters. It has been reported that the issues of stability can be addressed by using the control signal to output voltage transfer function of the converters, named G_{VC}, for such class of converters. G_{VC} can be mathematically derived using describing-function approach to include the effects of side-band harmonics of the pulsewidth modulation (PWM) modulator. This is essential for modeling the control behavior of the COT converter class. However, the actual G_{VC} can deviate significantly from the derived ideal model. Therefore, a measured G_{VC} transfer function is important for real-world stability predictions. G_{VC} measurement, however, is often not feasible because the points of measurements are physically inaccessible due to integrated control circuit implementation. In this article, a realistic G_{VC} extraction method is proposed for each of the four commonly used COT schemes. Based on the measured G_{VC}, a procedure to predict the stability boundary is proposed and verified.**

***Index Terms*—Buck converter, constant ON-time, control-to-output, current-mode COT, hybrid COT, ripple-based, V^2 control.**

I. Introduction

In RECENT years, converters employing ripple-based constant ON-time (COT) controllers have been extensively used, especially in mobile device applications. It features simple circuit, low cost, and high efficiency under light-load stand-by conditions. It allows the converters to meet the ever-tightening energy-efficiency requirements while preserving other necessary features. There are several schemes reported, based on the same control principle [1]–[3].

In this article, the issues of feedback control stability will be the focus of such a class of converters. However, the traditional well-known small-signal average model [4] is not applicable here. Due to the fact that the output switching-frequency ripple voltage is directly involved in the duty-cycle modulation of the COT class of converters, the effects of side-band harmonics must be included in the modulation gain modeling. Reference [5] reported a pioneering effort using describing-function approach to resolve the issue.

Manuscript received April 17, 2020; revised July 20, 2020 and September 30, 2020; accepted November 11, 2020. Date of publication November 25, 2020; date of current version February 5, 2021. Recommended for publication by Associate Editor G. Moschopoulos. *(Corresponding author: Ching-Jan Chen.)*

The authors are with the National Taiwan University, Taipei 100225, Taiwan (e-mail: brian.tinghung.wang@gmail.com; chendy@ntu.edu.tw; chenjim@ntu.edu.tw; e7226176@gmail.com).

Color versions of one or more of the figures in this article are available at https://doi.org/10.1109/TPEL.2020.3040553.

Digital Object Identifier 10.1109/TPEL.2020.3040553

In [5], the control-to-output transfer function G_{VC} was derived under ideal conditions, from which the stability issues were then determined by examining the characteristic roots of the idealized closed-form G_{VC} function. Under practical conditions, however, G_{VC} may have noticeable discrepancy due to nonideal factors such as the parasitic elements of the components and PCB, the propagation delay of the feedback loop elements, and the temperature effects. Therefore, it is important to have a hardware measurement of G_{VC} to achieve a realistic stability prediction. However, a G_{VC} measurement is usually not feasible, because the point of measurement is not physically accessible due to integrated circuit (IC) implementation of the control circuits. Since the use of IC controller is so pervasive, and the measurement of G_{VC} is always necessary, it is desirable to find a practical solution to this problem. In this article, a new method will be proposed and verified to address the issues. Relevant literatures about COT buck converters [6]–[21] will be referenced. Among these references, [6]–[13] are about the modeling of different types of COT configurations, and [14]–[21] are about up-to-date modified COT control circuits reported in recent years. These references will be cited at the proper places in Section II to point out the differences and significance of this article.

In Section II, a basic review will be given for the four common COT control schemes, and an explanation of the stability results will be derived from the describing function approach reported in [5]. Section III will provide the theoretical foundation for the proposed G_{VC} measurement methods for COT converters implemented with IC controllers. In Section IV, a stability prediction method will be developed based on the measured G_{VC}, which is in frequency-domain format, as opposed to a closed-form function in the ideal model. Experimental comparisons will be made using the results from the two design methods, one based on the ideal model and the other based on the proposed method in [5]. In Appendix I, a list of symbol definitions is provided. A critical step to find out the stability parameters from the measured G_{VC} curves is derived in Appendix II.

II. Review of COT Control Circuit and Stability Issue

A. Review of COT Control Circuit Schemes

For COT controlled buck converters, there are four control circuit schemes: RBCOT control, V^{2}COT control, CMCOT control, and hybrid COT control [6]–[13].

Fig. 1(a) shows the diagram of a basic voltage-mode ripple-based COT, which is usually named as RBCOT. In RBCOT,

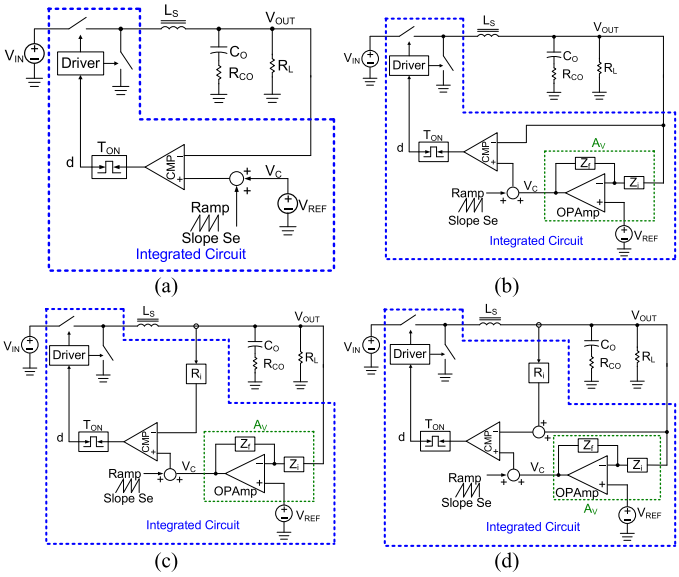

Fig. 1. Constant ON-time control schemes of buck converter. (a) RBCOT. (b) V^2COT. (c) CMCOT. (d) hybrid COT control.

the output voltage ($V_{\rm OUT}$), including the ripple is directly compared with the reference voltage ($V_{\rm REF}$) to achieve modulation. Another embodiment of the voltage-mode COT control is depicted in Fig. 1(b), commonly known as V^2COT, where the V^2 means two voltage loops: the inner voltage loop of direct $V_{\rm OUT}$ feedback, and the outer voltage loop of compensated $V_{\rm OUT}$ feedback. Fig. 1(c) shows the diagram of current-mode COT (CMCOT) control, which typically contains two control loops: the inner current loop and the outer voltage loop. The pulsewidth modulation (PWM) of CMCOT is achieved by comparing the inductor current signal with the control signal (V_C), where V_C is generated by the compensated output voltage feedback. The Hybrid COT control as depicted in Fig. 1(d) is the combination of voltage-mode COT control and current-mode COT control: one current loop, one voltage loop, and one compensated voltage loop to generate the control signal.

In Fig. 1, the circuit enclosed in each of the dashed blue boxes is usually implemented in an IC, which contains the power switches, the driver circuit, and the feedback control circuit.

B. Review of G_{VC} *Model and Ramp Design Criteria for an Ideal System*

1) G_{VC} *Model:* The conventional state-space-average method cannot be used to analyze a COT control modulator due to the reason that the harmonics and sidebands at the pulse width modulator output are carried into the control loop. $G_{\rm VC}$ ($\equiv v_{\rm out}/v_c$) function plays a critical role in revealing the control stability and transient response characteristics of the control system. Reference [5] reported a pioneering effort using describing-function, and the following literatures [7]–[13] inherited the same concept and created dedicated models for four control circuit schemes of COT converter. The describing function approach was applied in [7] and [8] to obtain the $G_{\rm VC}$ for RBCOT buck converters, and the $G_{\rm VC}$ derivation of improved RBCOT topologies with virtual inductor current or adaptive ramp are introduced in [9] and [10]. A three terminal switch model based on $G_{\rm VC}$ derivation of CMCOT was proposed in [11]. In [12] and [13], the performance comparison of digital control schemes of V^2COT and hybrid COT were introduced by derivation of $G_{\rm VC}$ transfer functions. With rigorous mathematics, a closed-form $G_{\rm VC}$ was obtained which is accurate up to switching frequency. The $G_{\rm VC}$ expression is given as follows:

$$G_{\rm VC}(s) \equiv \frac{v_{\rm out}(s)}{v_c(s)} = \frac{1+\frac{s}{Q_2\cdot\omega_2}+\frac{s^2}{{\omega_2}^2}}{\left(1+\frac{s}{Q_{e1}\cdot(\beta\cdot\omega_2)}+\frac{s^2}{(\beta\cdot\omega_2)^2}\right)\cdot\left(1+\frac{s}{Q_{e2}\cdot({\omega_2}/{\beta})}+\frac{s^2}{({\omega_2}/{\beta})^2}\right)}. \tag{1}$$

All the symbols in the equations are defined in Appendix I. Among the parameters in (1), Q_2 ($= 2/\pi$) and ω_2 ($= \pi/T_{\rm SW}$) are constants. Q_{e1} and Q_{e2} are two quality factors of the two pairs of poles, and β is a factor influencing the corner frequency of the two pairs of poles. S_e, the slope of the external ramp, is a parameter hidden in the expressions of Q_{e1} and Q_{e2}, which will be shown later along with the β expression. There are two sets of expressions for Q_{e1}, Q_{e2}, and β, and the different expressions are depending on whether S_e is greater or smaller than the breaking point's external ramp slope $S_{\rm e\_K}$. An explanation will be given later for the physical significance of $S_{\rm e\_K}$, and the expression is given in (2) in which α is a coefficient defined in (3)

$$S_{e\_K} \equiv \frac{(1-2\cdot\alpha+D)^2}{16\cdot\alpha}\cdot S_f \tag{2}$$

$$\alpha \equiv \frac{R_{\rm CO}\cdot C_O}{T_{\rm SW}}. \tag{3}$$

In summary, the expression for Q_{e1}, Q_{e2}, and β are given as follows [8].

1) If $S_e \le S_{\rm e\_K}$, then

$$\beta = 1$$

$$Q_{e1} = \frac{4}{\pi}\cdot\frac{1}{1+2\cdot\alpha-D+\sqrt{(1-2\cdot\alpha+D)^2-16\cdot\alpha\cdot({S_e}/{S_f})}}$$

$$Q_{e2} = \frac{4}{\pi}\cdot\frac{1}{1+2\cdot\alpha-D-\sqrt{(1-2\cdot\alpha+D)^2-16\cdot\alpha\cdot({S_e}/{S_f})}}. \tag{4}$$

2) If $S_e \ge S_{e\_K}$, then

$$\beta = \frac{\sqrt{4+Y}+\sqrt{Y}}{2}$$

$$Q_{e1} = Q_{e2} = \frac{2}{\pi}\cdot\frac{1}{1+2\cdot\alpha-D}\cdot\left(\beta+\frac{1}{\beta}\right)$$

where

$$Y = \frac{\pi^2}{4} \cdot \left[\left(2 \cdot \frac{S_e}{S_f} + 1 \right) \cdot \alpha - \frac{D}{2} \right] - 2 + \frac{1}{2} \cdot \sqrt{\left\{ \frac{\pi^2}{2} \cdot \left[\left(2 \cdot \frac{S_e}{S_f} + 1 \right) \cdot \alpha - \frac{D}{2} \right] + 4 \right\}^2 - \pi^2 \cdot (1 - 2 \cdot \alpha + D)^2}. \quad (5)$$

An explanation of S_{e_K} will be given below. From (1), one can see that there are two pairs of poles. The two pairs of poles move in the complex plane as the S_e value varies, resulting in a root-locus plot. According to [8], if the S_e value is smaller than a break-point value S_{e_K}, the two pairs of poles move but stick together at $f_{sw}/2$ line as S_e varies. As S_e is increased passing the breaking point S_{e_K}, the two pairs of poles' trajectories split in the complex plane. The behavior of the poles affects the converter stability and transient response. The expression for S_{e_K} is given in (2).

2) Stability and Transient Response: From G_{VC} transfer function (1), stability condition can be determined by examining the existence of right half plane (RHP) poles, i.e., examining negative quality factors in (1). From [8], (6) is the criteria for stability, where S_e is the actual slope of the external ramp, and S_{e_C} is the minimum required external ramp slope to achieve a stable COT buck converter design

$$S_e \geq S_{e\_C} \equiv \frac{D - 2 \cdot \alpha}{4 \cdot \alpha} \cdot S_f. \quad (6)$$

Too small S_e ($S_e < S_{e\_C}$) results in instability, but too large S_e is not desirable, because that leads to too large quality factor and thus poor output voltage performance when a step-load occurs.

In summary from prior studies of COT stability, two criteria are concluded for a good COT ramp design: (6) for stable control loop without RHP poles, and $S_{e\_K} < S_e < 4 \cdot S_{e\_K}$ for acceptable transient performance [8].

C. Issues of COT Stability on Real Systems

1) Issue of Nonideal Parameter Variations: The first issue for COT stability judgment on real systems is the discrepancy between ideal models and real circuits due to nonideal parameter variations.

The G_{VC} mathematical model described in Section II-B can be used to figure out the range of S_e value for stability margin and step-load output transient response for an ideal system. However, the G_{VC} for a real system can be significantly different from an ideal system. Fig. 2 shows an example of G_{VC} discrepancy between a real circuit measurement result and an ideal model from [5]. The working conditions and component values are given in Table I. The measurement was conducted using a network analyzer, which provides a perturbing signal at the V_C terminal and measures v_{out}/v_c gain.

The discrepancy comes from accumulation of effects of sensing amplifier nonlinearity, comparator delay, printed circuit board impedance, component impedance variation during system operation, and so forth. In [14], comparator delay was incorporated for stability prediction in RBCOT circuit, but the signal propagation delay time of the feedback circuit is difficult to predict. In [15], a digital V^2COT control with hybrid capacitor current ramp compensation scheme is proposed, but the stability verification was done by simulation only. In [16], a theoretical frequency-domain small signal model of the same circuit was derived, but a hardware verification of stability is lacking, and the nonideal factors cannot be incorporated in the ideal model.

2) Issue of Inaccessible Control Terminal Due to IC Implementation: The second issue for COT stability judgment on real systems is that the G_{VC} cannot be directly measured due to inaccessible V_C terminal in IC implementation as shown in Fig. 1 in dashed blue boxes.

In RBCOT G_{VC} models discussed in [7]–[10], hardware measurement is possible only for a controller using discrete

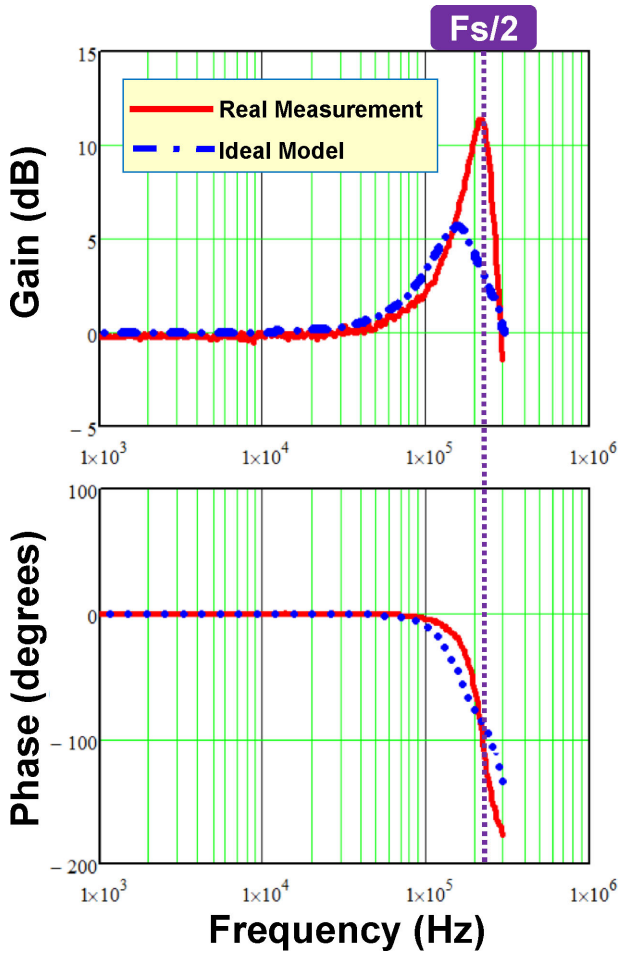

Fig. 2. G_{VC} discrepancy between a real circuit measurement and an ideal model.

TABLE I
CIRCUIT PARAMETERS FOR EXPERIMENTAL VERIFICATION

Input voltage V_{IN}	12V
Output voltage V_{OUT}	1V
Switching frequency f_{SW}	450KHz
Output inductor L_S	220nH
Output MLCC capacitor R_{CO} and C_O	MLCC 22μF/3mΩ, 11pcs (P/N: GRM21BR60J226ME39)
Output load resistor R_L	1Ω
Slope of external ramp S_e	5454V/s

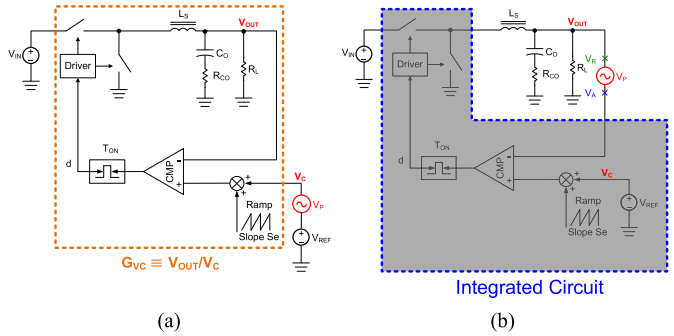

Fig. 3. Comparison of $G_{\rm VC}$ measurement of RBCOT buck converter. (a) With discrete control components. (b) With IC implementation.

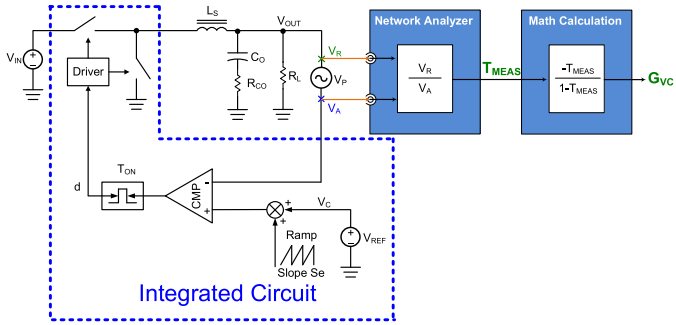

Fig. 4. Proposed $G_{\rm VC}$ Extraction of RBCOT buck converter.

components as shown in Fig. 3(a) in which a perturbation signal v_P is inserted, and the $G_{\rm VC}$ can be found by $v_{\rm OUT}/v_C$. However, most controllers are implemented in IC in which the control terminal V_C is inside the IC and not accessible as shown in Fig. 3(b). Similar issue can be found in V^2COT and hybrid COT in [12] and [13], that the control terminal V_C is not practically accessible in most real circuits. In real circuits of V^2COT and hybrid COT, the perturbation signal can only be inserted in the output voltage feedback path. Several recent papers on modified COT control scheme strategies will be described below. In [17], a so-called AQCOTCM control scheme to improve step-load transient response is described. In [18], a new current sensing scheme is proposed to actively sense the low-side MOSFET current to generate the ramp signal for performance improvements about stability, dc offset, and output impedance. In [19], a capacitor ripple-coupling COT scheme is proposed to reduce the quiescent current of the control IC. In [20], a control scheme with optimized on-time control circuit and body-diode control circuit was proposed to improve load transient response. In [21], a novel state-trajectory control method to improve the single-cycle response of V^2COT control is proposed. For all the aforementioned five schemes, experimental measurement of $G_{\rm VC}$ is not possible when implemented in IC for the same reason mentioned earlier in this article. Up to date, there is no experimentally-based stability prediction of real-world COT buck converter circuit ever reported. This fact further points out the uniqueness and the importance of the method proposed in this article.

In Fig. 3(b), a perturbation signal v_P is inserted, and the Bode plot $T_{\rm MEAS}$ (defined as v_R/v_A) can be measured, which is very much like the conventional open loop measurement used in traditional average models [22]. However, this T_{MEAS} cannot be used for stability judgment for converters with COT control. As mentioned in Section I, the output voltage $V_{\rm OUT}$ signal in a COT control is fed directly to the modulator resulting in high content of sideband harmonics that propagate around the loop. And, such a loop measurement result is meaningless and cannot be used for stability judgment. As a comparison, in conventional constant-frequency control schemes, a low-pass compensator circuit is in the loop that essentially filters out the high-frequency sideband harmonics of the $v_{\rm OUT}$ signal before going through the modulator, and these results in basically a single-frequency signal circulating around the loop [23]. For this reason, a describing function approach was first reported in [5] to derive a theoretical $G_{\rm VC}$ function to deal with COT control stability issue.

III. Proposed Extraction Methods for GVC When the COT Controller is an IC

As mentioned in Section II, there can be significant discrepancy between the theoretical $G_{\rm VC}$ and the measured $G_{\rm VC}$. As also mentioned, measuring a real circuit $G_{\rm VC}$ is not apparent if the COT controller is in integrated form which is almost universally used today. In this section, a method will be developed under such circumstances for each of the four COT control schemes given in Fig. 1. Theoretical foundation will be provided, and the results will be verified.

A. G_{VC} Extraction of RBCOT

Fig. 4 shows the circuit diagram of RBCOT buck converter $G_{\rm VC}$ extraction by a network analyzer. The first step of $G_{\rm VC}$ extraction is to measure the loop response $T_{\rm MEAS}$ by inserting a perturbation signal v_P into the feedback loop, where $T_{\rm MEAS}$ is the ratio of the returned signal v_R to the perturbation input signal v_A. Note that as discussed in Section II-C, although the $T_{\rm MEAS}$ measurement method is similar to traditional open-loop gain measurement, the measured $T_{\rm MEAS}$ cannot directly be used to judge COT control loop stability. On the contrary, since the measured $T_{\rm MEAS}$ contains all the sideband harmonics of the perturbed control loop, the measured $T_{\rm MEAS}$ can be used to extract $G_{\rm VC}$ by the following proposed calculation steps.

After measured $T_{\rm MEAS}$, the second step to extract $G_{\rm VC}$ is given below by using (7). The calculation procedures from $T_{\rm MEAS}$ to $G_{\rm VC}$ are by using mathematical calculators such as Excel to calculate the complex numbers at every frequency point [24]. The calculation results of $G_{\rm VC}$ at every frequency point can then be plotted into a Bode plot

$$G_{\rm VC} = \frac{-T_{\rm MEAS}}{1 - T_{\rm MEAS}}. \tag{7}$$

It can be seen from the above description that the two measuring points v_R and v_A are outside the controller IC and physically accessible. In the rest of this paragraph, derivation of (7) will be presented, and its accuracy will be verified.

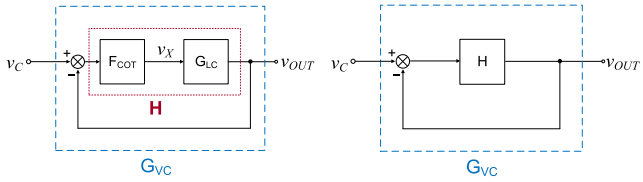

Fig. 5. (a) RBCOT block diagram. (b) Simplified RBCOT block diagram.

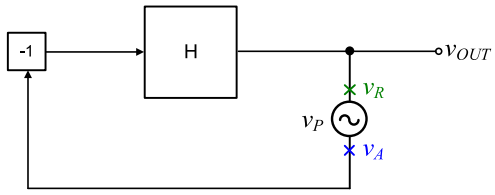

Fig. 6. Small-signal block diagram for G_{VC} extraction of RBCOT buck converter (excluding the Network Analyzer and Math calculation blocks).

Fig. 5(a) shows the G_{VC} definition by a simplified small-signal block diagram of RBCOT in which F_{COT} is the RBCOT modulator's transfer function $v_X/(v_C - v_{OUT})$, and G_{LC} is the LC filter's transfer function v_{OUT}/v_X. Note that the effect of the external ramp S_e is incorporated in F_{COT}. By combining F_{COT} and G_{LC} into the H block, a further simplified block diagram is shown in Fig. 5(b). Equation (8) can be derived from Fig. 5(b),

$$G_{VC} = \frac{v_{out}}{v_c} = \frac{H}{1+H}. \tag{8}$$

From (7) and (8), it can be seen that if H is equal to $(-T_{MEAS})$, then the proposed RBCOT G_{VC} extraction method is validated.

In the following paragraph, it will be proved that H is equal to $(-T_{MEAS})$.

For the G_{VC} extraction circuit in Fig. 4, the equivalent small-signal block diagram is given in Fig. 6. The voltage feedback loop in Fig. 6 is different from Fig. 5 (b), because comparing Fig. 4 with Fig. 3(a), the perturbation v_P in Fig. 4 is inserted between v_{OUT} and the negative input terminal of the comparator, and the ac signal of V_C is zero. From Fig. 6, one can obtain (9). Equation (10) can be obtained by using the definition of T_{MEAS} and (9).

$$(-v_A) \cdot H = v_R \tag{9}$$

$$T_{MEAS} \equiv \frac{v_R}{v_A} = (-H). \tag{10}$$

Equation (10) proves that H is indeed equal to $(-T_{MEAS})$. Therefore, the proposed method of Fig. 4 is theoretically valid. Equation (7) is finally proved by combining (8) and (10).

A simulation result by using SIMPLIS also verifies the proposed method, as shown by Fig. 7. The working conditions and component values of the simulation are given in Table I. The dashed red curve is the result using the proposed G_{VC} extraction method, and the solid green curve is the simulated G_{VC} by directly probing v_{OUT}/v_C. The two curves coincide with each other.

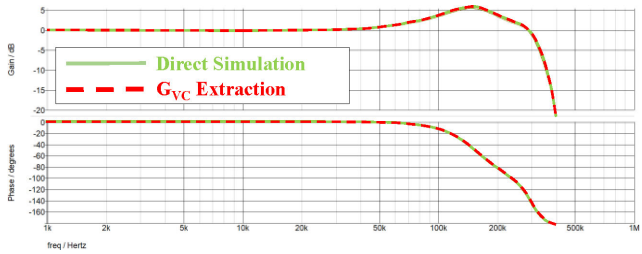

Fig. 7. SIMPLIS simulation result of RBCOT G_{VC} extraction.

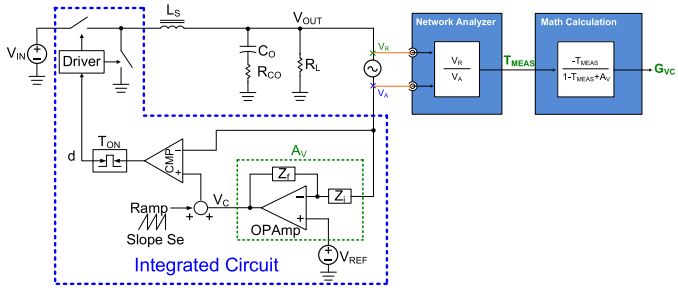

Fig. 8. Proposed G_{VC} Extraction of V^2COT buck converter.

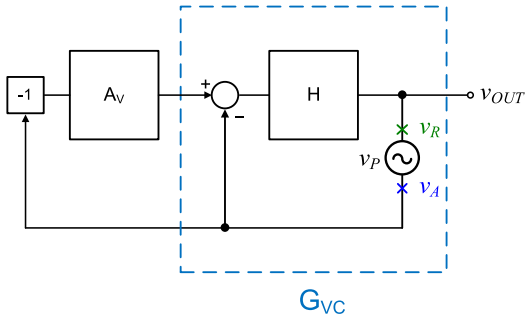

Fig. 9. Small-signal block diagram for G_{VC} extraction of V^2COT buck converter (excluding the Network Analyzer and Math calculation blocks).

B. G_{VC} Extraction of V^2COT

Fig. 8 shows the circuit diagram of the proposed G_{VC} extraction for a V^2COT buck converter. Fig. 9 shows the small-signal block diagram of V^2COT buck converter G_{VC} extraction, where A_V is the compensator transfer function as depicted in Fig. 8 in the dashed green box. From the dashed blue box of G_{VC} in Fig. 9, one can conclude that (8) also holds for V^2COT, because the inner loop structure of V^2COT is the same as the single loop structure of RBCOT. From Fig. 9, one can obtain (11). Equation (12) can be obtained by using (10) and (11)

$$[(-v_A) \cdot A_V - v_A] \cdot H = v_R \tag{11}$$

$$T_{MEAS} \equiv \frac{v_R}{v_A} = [-(1+A_V)] \cdot H. \tag{12}$$

Substituting H in (8) by using (12), one can obtain the relationship of G_{VC} and T_{MEAS} in V^2COT

$$G_{VC} = \frac{-T_{MEAS}}{1 - T_{MEAS} + A_V} \tag{13}$$

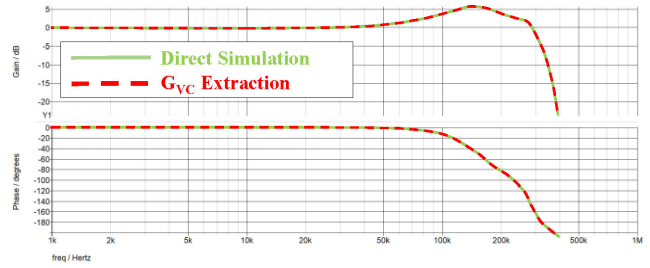

Fig. 10. SIMPLIS simulation result of V^2COT G_{VC} extraction.

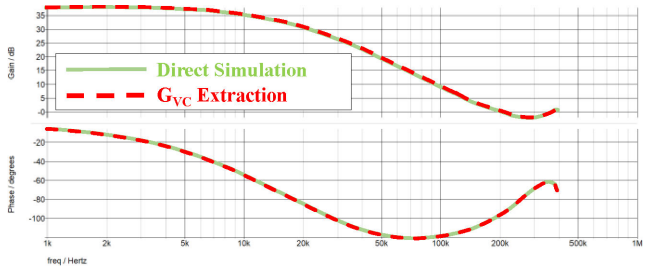

Fig. 13. SIMPLIS simulation result of CMCOT G_{VC} extraction.

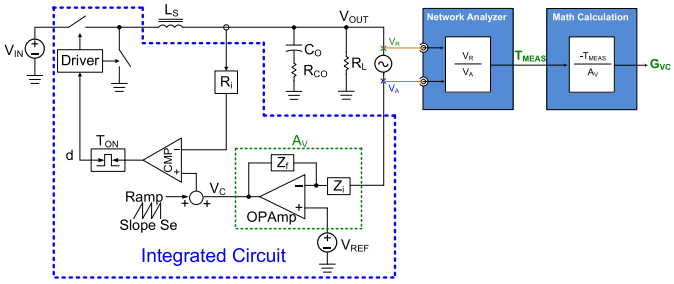

Fig. 11. Proposed G_{VC} Extraction of CMCOT buck converter.

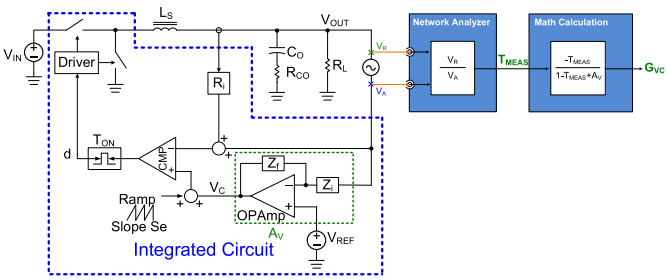

Fig. 14. Proposed G_{VC} Extraction of hybrid COT buck converter.

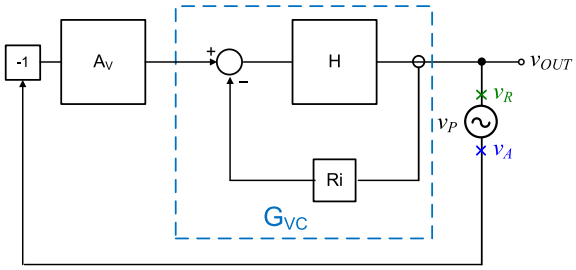

Fig. 12. Small-signal block diagram for G_{VC} extraction of CMCOT buck converter (excluding the Network Analyzer and Math calculation blocks).

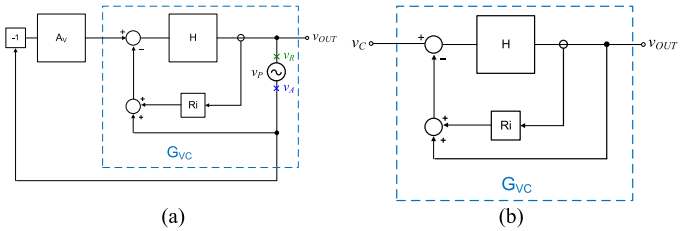

Fig. 15. (a) Small-signal block diagram for G_{VC} extraction of hybrid COT buck converter. (b) G_{VC} definition in hybrid COT.

where v_R is the returned signal, and v_A is the perturbation input signal.

Similarly, the proposed G_{VC} extraction method for V^2COT is verified by the simulation result shown in Fig. 10. The working conditions and component values of the simulation are given in Table I, and the compensator A_V is a type-I compensator with $R = 100$ KΩ and $C = 100$ pF. The dashed red curve is the result of the proposed G_{VC} extraction by (13), and the solid green curve is the simulated G_{VC} by directly probing v_{OUT}/v_C.

C. G_{VC} Extraction of CMCOT

Fig. 11 shows the circuit diagram of CMCOT buck converter G_{VC} extraction, and Fig. 12 shows the small-signal block diagram of Fig. 11. For CMCOT structure, G_{VC} contains the inner current loop as shown by the dashed blue box in Fig. 12.

To find out G_{VC}, one can inject a perturbation signal v_P into the voltage feedback loop and obtain as follows:

$$T_{MEAS} \equiv \frac{v_R}{v_A} = -(G_{VC}) \cdot A_V \tag{14}$$

$$G_{VC} = \frac{-T_{MEAS}}{A_V}. \tag{15}$$

Similarly, the proposed G_{VC} extraction method for CMCOT is verified by the simulation result shown in Fig. 13. The working conditions and component values of the simulation are given in Table I, where the current sense gain is 1 mV/A, and the compensator A_V is a type-I compensator with $R = 100$ KΩ and $C = 5$ nF. The dashed red curve is the result of the proposed G_{VC} extraction by (15), and the solid green curve is the simulated G_{VC} by directly probing v_{OUT}/v_C.

D. G_{VC} Extraction of Hybrid COT

Fig. 14 shows the proposed G_{VC} extraction of a hybrid COT buck converter. In hybrid COT, as discussed in Section II, there are three control loops. In the proposed G_{VC} extraction, the perturbation signal can only be inserted into the output voltage feedback path as indicated in Fig. 14. The small-signal block diagram of Fig. 14 is depicted in Fig. 15(a). The perturbation signal goes through the inner loop of G_{VC} and the outer loop of compensator. The G_{VC} definition of the dashed blue box in Fig. 15(a) is analyzed in Fig. 15(b) as follows:

$$G_{VC} \equiv \frac{v_{OUT}}{v_C} = \frac{H}{1 + H + R_i \cdot H}. \tag{16}$$

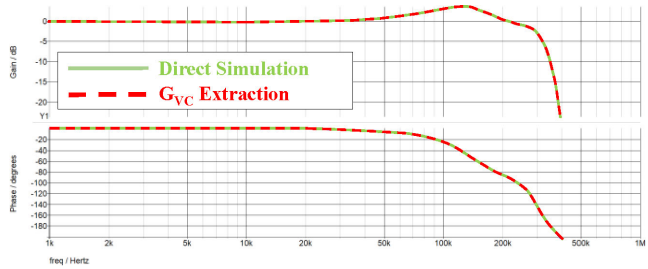

Fig. 16. SIMPLIS simulation result of hybrid COT $G_{\rm VC}$ extraction.

In Fig. 15(a), one can obtain

$$[(-v_A)\cdot A_V-(v_R\cdot R_i+v_A]\cdot H=v_R. \tag{17}$$

Equation (18) can then be derived as follows:

$$T_{\rm MEAS}\equiv\frac{v_R}{v_A}=\frac{-H\cdot(1+A_V)}{1+R_i\cdot H}. \tag{18}$$

Rearranging (18) leads to the following:

$$R_i\cdot H=\frac{-H\cdot(1+A_V)}{T_{\rm MEAS}}-1. \tag{19}$$

Substituting $R_i{\cdot}H$ in (16) using (19), one can obtain the relationship of $G_{\rm VC}$ and $T_{\rm MEAS}$ in hybrid COT

$$G_{\rm VC}=\frac{-T_{\rm MEAS}}{1-T_{\rm MEAS}+A_V}. \tag{20}$$

Note that (20) is the same as (13). In Figs. 9 and 15(a), the inner loop $G_{\rm VC}$ and the outer voltage loop are both perturbed by the inserted perturbation signal, so the relationships between the measured $T_{\rm MEAS}$ and $G_{\rm VC}$ are the same for both V^2COT and hybrid COT.

The proposed $G_{\rm VC}$ extraction method for hybrid COT is verified by the simulation result shown in Fig. 16. The working conditions and component values of the simulation are given in Table I, where the current sense gain is 1 mV/A, and the compensator $A_{\rm V}$ is a type-I compensator with $R=100$ KΩ and $C=100$ pF. The dashed red curve is the result of the proposed $G_{\rm VC}$ extraction by (20), and the solid green curve is the simulated $G_{\rm VC}$ by directly probing $v_{\rm OUT}/v_C$.

E. Experimental Verification of G_{VC} *Extraction*

A hardware RBCOT prototype platform was built using discrete components for the verification of the proposed $G_{\rm VC}$ extraction method. Fig. 17 shows the platform arrangement which consists of two evaluation boards. The larger board on the left is an RT5073A (Richtek Corp.) evaluation board. It is a multichannel COT buck converter board, but only one channel was used in the experiments. The other board is a ramp circuit board which generates external ramp voltage to be summed with the $V_{\rm REF}$ to provide the signal to the positive node of the RBCOT comparator as the circuit diagram shows. The working conditions and component values are given in Table I.

To obtain $G_{\rm VC}$ using the proposed $G_{\rm VC}$ extraction method in Section III-A, the first step is to measure $T_{\rm MEAS}$. The Network

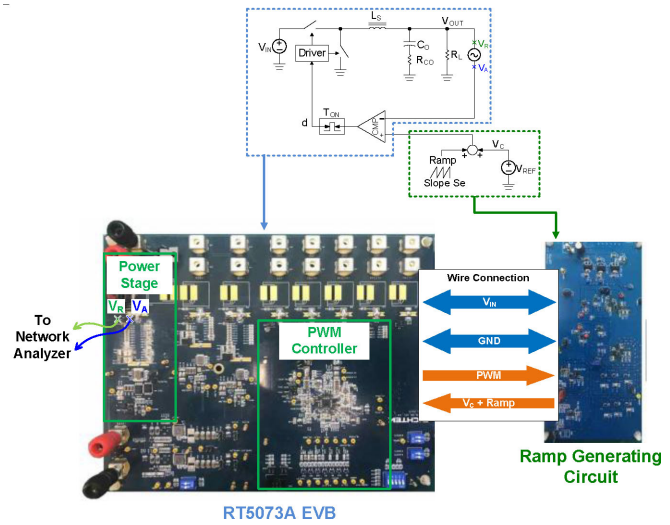

Fig. 17. Prototype platform for experimental verification.

Analyzer used was Omicron Bode 100 [25]. The perturbation source level is set at -20 dBm, the attenuator settings at Receiver 1 and 2 are both 10 dB, the logarithmic frequency sweeping starts from 1 KHz and stops at 1 MHz, and the number of sweeping points is 401 points.

Then, $G_{\rm VC}$ can be obtained by substituting the measured data $T_{\rm MEAS}$ into (7), noticing that $T_{\rm MEAS}$ is a complex number at each frequency point. Using mathematical calculators, the $G_{\rm VC}$ extraction result can be found and is shown by the dashed red curve in Fig. 18. Because of the discrete nature of the hardware circuit, both measurement ports are accessible, and a direct-measurement of $G_{\rm VC}$ is possible by following the diagram given in Fig. 3(a). The result of $G_{\rm VC}$ direct-measurement is shown by the solid blue curve in Fig. 18. The two curves agree very well.

IV. Stability Prediction From the Measured $G_{\rm VC}$

The theoretical $G_{\rm VC}$ expression (1) is a closed-form function, so the stability and transient response issues can be predicted from the eigen-values of the expression. For the measured $G_{\rm VC}$, it is a Bode Plot, not a closed form expression, and the extraction of stability parameters is not apparent. In this section, equations will be derived to find the critical control parameters from the measured $G_{\rm VC}$.

As mentioned in Section II, $G_{\rm VC}$ characteristics affect feedback stability and step-load transient performance of the COT converters. The design objective of the control is to find a proper slope of the external ramp S_e to maintain stability and achieve good transient performance. For ideal $G_{\rm VC}$, the two ideal parameters $S_{\rm e\_K\_ideal}$ and $S_{\rm e\_C\_ideal}$, which are given, respectively, by (2) and (6), play important roles in system stability and transient performances [8].

In Section A below, a description will be given to find $S_{\rm e\_C\_real}$ and $S_{\rm e\_K\_real}$ from a measured $G_{\rm VC}$. In Section B, a step-by-step practical design example will be used for an RBCOT buck converter to illustrate the description given in

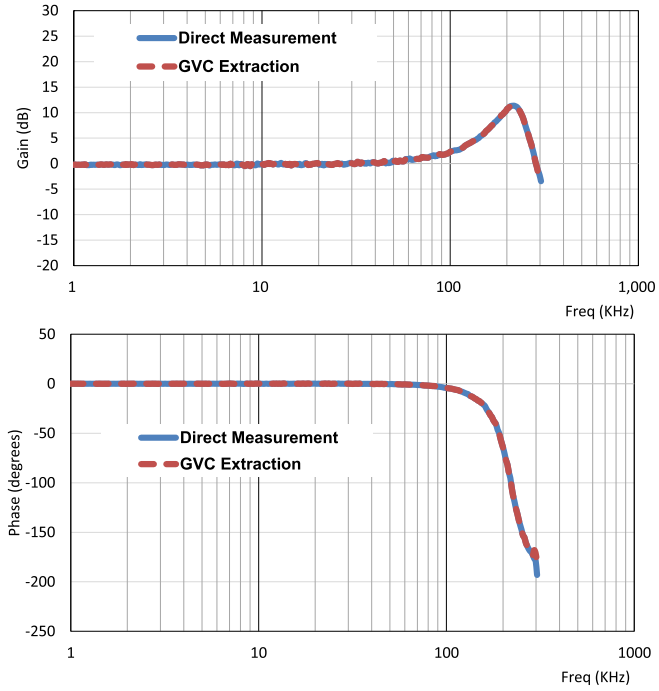

Fig. 18. Experimental verification of G_{VC} extraction method for an RBCOT buck converter. Perturbation source level −20 dBm, attenuator Receiver 1 and 2 both 10 dB, frequency sweeping 1 KHz to 1 MHz, and 401 sweeping points.

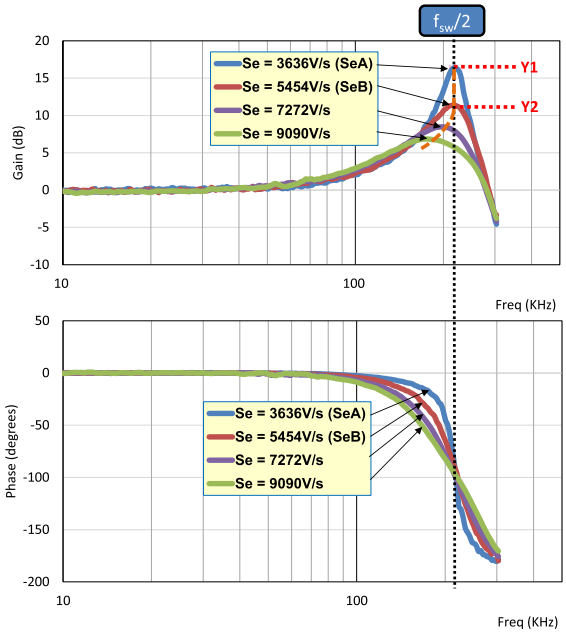

Fig. 19. $|G_{VC}|_A$ (Y1) and $|G_{VC}|_B$ (Y2) measurement example for G_{VC} extraction method for COT buck converter.

Section A. In Section C, a comparison of end results will be made between the proposed method and the ideal model currently used.

A. Calculation of the Equivalent $S_{e\_C\_real}$ and $S_{e\_K\_real}$ from the Measured G_{VC}

The first step is to measure two different G_{VC} curves, G_{VC_A} and G_{VC_B}, based on two different ramp slope settings S_{eA} and S_{eB}. The second step is to obtain the amplitude values at half-switching-frequency ($f_{SW}/2$) point, named $|G_{VC}|_A$ and $|G_{VC}|_B$. Take Fig. 19 as an example, for the blue curve ($S_{eA} = 3636$ V/s) and the red curve ($S_{eB} = 5454$ V/s), $|G_{VC}|_A$ is marked as *Y1* and $|G_{VC}|_B$ is marked as *Y2*. $S_{e\_K\_real}$ and $S_{e\_C\_real}$ can then be calculated by using (21) and (22), respectively. The parameter definitions of (21) and (22) are listed in Appendix I, and their detailed derivation are given in Appendix II.

$$S_{e\_K\_real} = \frac{\left[\frac{S_{eB}}{|G_{VC}|_A} - \frac{S_{eA}}{|G_{VC}|_B} - \frac{\pi^2}{4}\cdot Q_2\cdot(S_{eB}-S_{eA})\right]^2}{\pi^2\cdot Q_2\cdot(S_{eB}-S_{eA})\cdot\left(\frac{1}{|G_{VC}|_B}-\frac{1}{|G_{VC}|_A}\right)} \tag{21}$$

$$S_{e\_C\_real} = \frac{S_{eB}\cdot|G_{VC}|_B - S_{eA}\cdot|G_{VC}|_A}{|G_{VC}|_B - |G_{VC}|_A}. \tag{22}$$

It should be noted that (21) and (22) are valid only if S_e is greater than $S_{e\_C\_real}$, which is the condition for stability according to (6). As explained in Section II, the pole pairs of G_{VC} stick together at half-switching frequency line as long as S_e is smaller than the "breaking" point $S_{e\_K\_real}$ [8]. This means there is a pronounced peak near the half-switching frequency point as shown in the Fig. 19. If $S_e > S_{e\_K\_real}$, the two pole pairs split and drift away from the half-switching frequency point, and the G_{VC} plot exhibits lower peak amplitude. In other words, to use (21) and (22), the S_e selected in the measurement experiments must be smaller than $S_{e\_K\_real}$. This will be seen more clearly in Appendix II.

B. Design Example of Finding Realistic $S_{e\_K\_real}$ and $S_{e\_C\_real}$ of a Real System

A design example of an RBCOT buck converter will be given below based on the explanation given in the previous Section. Table I provides the circuit working conditions and component values. This specification is a practical one from a commercial product.

Step 1: Calculate $S_{e\_K\_ideal}$ and $S_{e\_C\_ideal}$ according to (2) and (6). $S_{e\_K\_ideal} = 5496$ V/s and $S_{e\_C\_ideal} = 982$ V/s.

Step 2: Choose S_{eA} and S_{eB} with proper margin. Both must be larger than $S_{e\_C\_ideal}$ and smaller than $S_{e\_K\_ideal}$. Choose $S_{eA} = 3636$ V/s and $S_{eB} = 5454$ V/s.

Step 3: Use the chosen S_{eA} in the circuit and measure $|G_{VC}|_A = 16.24$ dB $= 6.486$. Similarly, use S_{eB} in the circuit and measure $|G_{VC}|_B = 11.24$ dB $= 3.648$.

Step 4: Substitute the chosen S_e values and the measured $|G_{VC}|$ values into (21) and (22), and calculate $S_{e\_K\_real} = 6618$ V/s and $S_{e\_C\_real} = 1300$ V/s.

C. Comparison of the Results: The Proposed Versus the Ideal Model

1) Comparison of Stability Boundary: For a stable system, the circuit's S_e must be larger than the predicted value. From

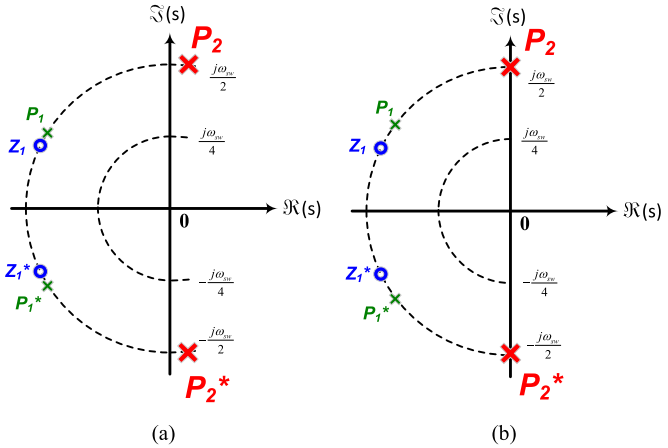

Fig. 20. $G_{\rm VC}$ pole-zero location comparison of different S_e design targets between the proposed method and ideal model. (a) Ramp is set as $S_{\rm e\_C\_ideal}$. (b) Ramp is set as $S_{\rm e\_C\_real}$.

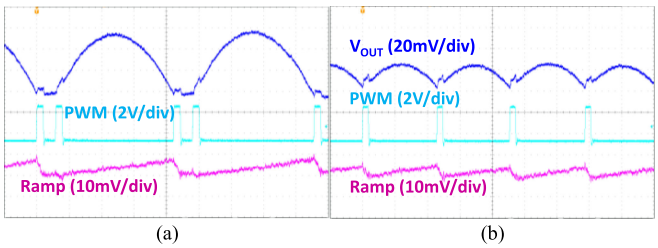

Fig. 21. $S_{\rm e\_C\_real}$ experimental verification. (a) S_e = 1200 V/s. (b) S_e = 1400 V/s.

Section IV-B in Steps 1 and 4, $S_{\rm e\_C\_ideal}$ = 982 V/s and $S_{\rm e\_C\_real}$ = 1300 V/s. This means the ideal model prediction is too optimistic, and the percentage error is about 30%.

This can also be seen from the pole-zero plots of the $G_{\rm VC}$ in Fig. 20 for the two different S_e values obtained in Section IV-B Steps 1 and 4, which are $S_{\rm e\_C\_ideal}$ = 982 V/s and $S_{\rm e\_C\_real}$ = 1300 V/s. The $S_{\rm e\_C\_ideal}$ is used in Fig. 20(a), and the $S_{\rm e\_C\_real}$ is used in Fig. 20(b). There are many poles and zeros, but the complex conjugate pole pair P_2 is the main focus for stability. In Fig. 20(a), P_2 pair is on the right-half plane that implies instability. That means using the design result based on the ideal model is incorrect. However, in Fig. 20(b), using the design result based on the proposed method correctly predicts the stability boundary.

This is further proved in the experimental waveforms given in Fig. 21. In Fig. 21(a), S_e of 1200 V/s is used which is greater than ideal model prediction of $S_{\rm e\_C\_ideal}$ = 982 V/s, and (6) is satisfied. Therefore, the system should be stable as the ideal model predicts, but the real measurement waveforms show instability. This can be clearly seen from the PWM waveform which exhibits double pulse instability. So, the ideal model incorrectly predicts the stability boundary. On the contrary, the proposed prediction value of $S_{\rm e\_C\_real}$ of 1300 V/s correctly predicts the instability. In Fig. 21(b), the circuit S_e is set at 1400 V/s which is larger than $S_{\rm e\_C\_real}$ = 1300 V/s, and the system is supposed to

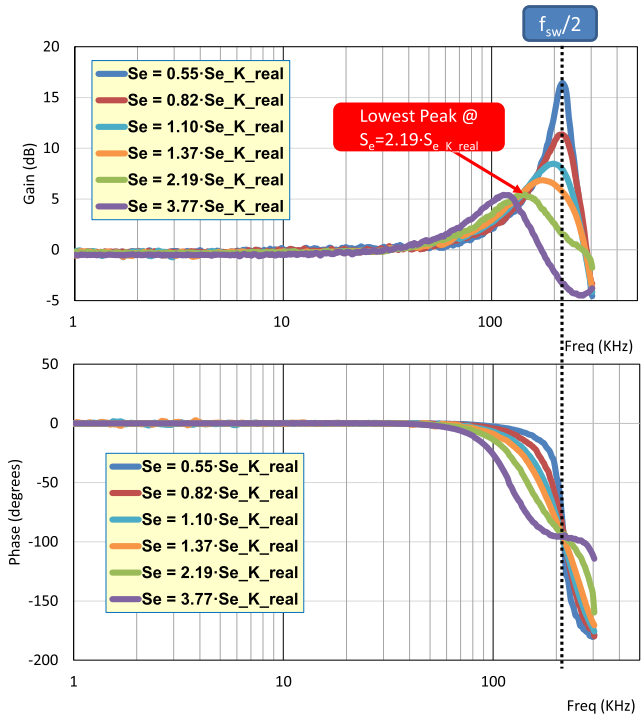

Fig. 22. $G_{\rm VC}$ measurement results with different S_e for finding the lowest gain peak amplitude in a real RBCOT circuit.

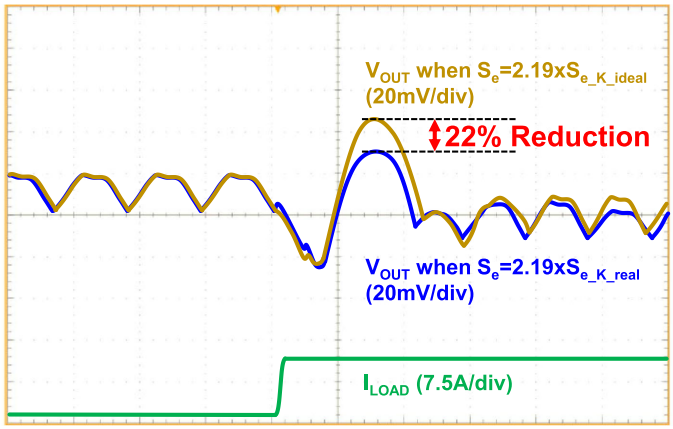

Fig. 23. Load step-up transient $V_{\rm OUT}$ comparison of different S_e design targets between the proposed method and ideal model.

be stable according to (6) and (22). Indeed, the system is stable as can be seen from the stable PWM waveform in Fig. 21(b).

2) Comparison of Step-Load Transient Response: As discussed in previous sections, the actual S_e must be greater than $S_{\rm e\_C\_real}$ to be stable, but this is not the only criterion for S_e design selection. The ratio of $S_e/S_{\rm e\_K\_real}$ makes difference in the step-load transient response [8]. Using the $S_{\rm e\_K\_real}$ = 6618 V/s from the design example in Section IV-B Steps 1 and 4, Fig. 22 plots the measurement results of $G_{\rm VC}$ for different $S_e/S_{\rm e\_K\_real}$ ratios, and the ratio of 2.19 results in the smallest peak amplitude, which also implies the smallest output impedance and roughly the smallest transient peak-to-peak voltage [8].

Using the results from the design example in Steps 1 and 4, $S_{\mathrm{e\_K\_ideal}} = 5496$ V/s and $S_{\mathrm{e\_K\_real}} = 6618$ V/s. Fig. 23 shows the comparison of the load transient experimental waveforms for the two S_e designs based on the proposed method and the ideal model, and the test condition is 10 A step load with 50 A/μs slew rate. A 22% reduction of the output voltage ring-back is achieved using the proposed method.

V. Conclusion

In the existing literatures, the discussions of stability issues for buck converters with COT controller family are based on a theoretical ideal G_{VC} model, which is totally different from the traditional average model. In this ideal model, not only the nonideal characteristics cannot be theoretically incorporated, but also a measurement of G_{VC} transfer function is not possible for controller circuits with integrated components. Since the COT controller circuits are almost universally implemented in IC nowadays, it is desirable to develop a method to overcome the shortcomings mentioned and to improve the design accuracy while boosting the end-design converter performances. The contributions of this article are to propose a methodology and to prove its validity experimentally for such a widely used converter-controller combination.

The proposed method consists of two major parts. One part is to extract the actual G_{VC} transfer function for the case of COT controller implemented in an IC. And, the other part is to mathematically derive real design boundaries from the measured G_{VC} to predict stability issues. Note that the measured G_{VC} is in frequency domain format, unlike the ideal model, which defines the G_{VC} in a closed-form function. The theoretical foundations and the experimental verification for both parts are provided.

A design example based on a commercial product specification was used to compare the proposed method and the theoretical model. The results indicated that the design based on theoretical models yielded an overly optimistic stability prediction. The design based on the proposed method improved the stability boundary accuracy by 30%. And, the converter step-load transient voltage ring-back is reduced by 22% by using the proposed design.

The proposed methods may be incorporated in a conventional network analyzer to make it easier for such measurements. In addition, the solution formulated in equation form allows possible tolerance analyses for mass production situations. This would facilitate the analysis and design of this family of converters.

Appendix I

Major parameters in this article are listed in the following table.

G_{VC}	The small-signal control-to-output transfer function $\equiv v_{OUT}/v_C$
Q_{e1}, Q_{e2}	Quality factors of G_{VC}'s two pairs of poles
β	A factor influencing the corner frequency of the two pairs of poles
Q_2	A constant equal to 2/π
ω_2	A constant equal to π/T_{SW}, radian of half-switching frequency
S_e	The slope of the external ramp
S_{e_K}	The ramp slope defining the break point of the G_{VC}'s two pairs of poles. When $S_e \le S_{e\_K}$, the two pole pairs stick together. When $S_e \ge S_{e\_K}$, the pole pair diverge
S_{e_C}	The critical ramp slope below which the system is unstable
$S_{e\_K\_real}$	While S_{e_K} is for an ideal circuit, $S_{e\_K\_real}$ is for a real circuit
$S_{e\_C\_real}$	While S_{e_C} is for an ideal circuit, $S_{e\_C\_real}$ is for a real circuit
v_A	Input signal at perturbation injection point
v_{R}	Return signal when the perturbation is injected into the circuit
T_{MEAS}	$v_{\mathrm{A}}/v_{\mathrm{R}}$ of the G_{VC} extraction method, the measured Bode plot when perturbation is inserted into the output voltage feedback loop
α	A factor = $(R_{CO}\cdot C_O)/T_{SW}$
D	Duty ratio
S_f	The slope of the inductor current falling edge
T_{SW}	Switching period
f_{SW}	Switching frequency
ω_{SW}	Radian of switching frequency
ω	Small-signal frequency variable in frequency domain
R_{CO}, C_O, L_S, R_L, V_{OUT}, V_C, F_{COT}, G_{LC}, H, R_{i}, A_{V}	Refer to Fig. 1, Fig. 4, and Fig. 5

Appendix II
Derivation of (21) and (22)

Equations (21) and (22) are two equations for obtaining $S_{\mathrm{e\_K\_real}}$ and $S_{\mathrm{e\_C\_real}}$ from a given measured G_{VC}. By substituting the variable s by $j\omega$, (1) can be rearranged as follows:

$$G_{\mathrm{VC}}(j\omega) = \frac{(1-\frac{\omega^2}{{\omega_2}^2}) + j\cdot\frac{\omega}{Q_2\cdot\omega_2}}{(1-\frac{\omega^2}{\beta^2\cdot{\omega_2}^2}-\frac{\beta^2\cdot\omega^2}{{\omega_2}^2}-\frac{\omega^2}{Q_{e1}\cdot Q_{e2}\cdot{\omega_2}^2}+\frac{\omega^4}{{\omega_2}^4}) + j\cdot(\frac{\omega}{Q_{e1}\cdot\beta\cdot\omega_2}-\frac{\beta\cdot\omega^3}{Q_{e1}\cdot{\omega_2}^3}+\frac{\beta\cdot\omega}{Q_{e2}\cdot\omega_2}-\frac{\omega^3}{Q_{e2}\cdot\beta\cdot{\omega_2}^3})} \tag{23}$$

By examining (23), as shown at the bottom of the previous page, one can see that if the following two conditions are met, i.e., $\omega = \omega_2$ and $\beta = 1$, (24) can be obtained which is much simplified.

$$|G_{\rm VC}(j\omega_2)| = \frac{Q_{e1} \cdot Q_{e2}}{Q_2} \tag{24}$$

$\omega = \omega_2$ and $\beta = 1$ is exactly the condition of $S_e \le S_{e\_K}$ explained in Section II-B-1. The $|G_{\rm VC}(j\omega_2)|$ in (24) is the value of $|G_{\rm VC}|$ at the half-switching frequency point. Equation (24) will be used to solve for the two hidden parameters $\alpha_{\rm real}$ and $S_{\rm f\_real}$ as explained below. By setting the external ramp slope in the circuit at a value $S_{\rm eA}$, one can measure the $|G_{\rm VC}|$ value at half-switching frequency point which is called $|G_{\rm VC}|_A$. Similarly, by setting ramp slope at $S_{\rm eB}$, one can measure $|G_{\rm VC}|_B$. Based on (24), (25) can be obtained in which $Q_{\rm e1A}$, $Q_{\rm e2A}$, $Q_{\rm e1B}$, and $Q_{\rm e2B}$ are expressed as (26) according to the definitions given by (4)

$$\begin{cases} |G_{\rm VC}|_A = \frac{Q_{e1A} \cdot Q_{e2A}}{Q_2} \\ |G_{\rm VC}|_B = \frac{Q_{e1B} \cdot Q_{e2B}}{Q_2} \end{cases} \tag{25}$$

where

$$\begin{aligned} Q_{e1A} &= \frac{4}{\pi} \\ &\cdot \frac{1}{1 + 2 \cdot \alpha - D + \sqrt{(1 - 2 \cdot \alpha + D)^2 - 16 \cdot \alpha \cdot (S_{eA}/S_f)}} \\ Q_{e2A} &= \frac{4}{\pi} \\ &\cdot \frac{1}{1 + 2 \cdot \alpha - D - \sqrt{(1 - 2 \cdot \alpha + D)^2 - 16 \cdot \alpha \cdot (S_{eA}/S_f)}} \\ Q_{e1B} &= \frac{4}{\pi} \\ &\cdot \frac{1}{1 + 2 \cdot \alpha - D + \sqrt{(1 - 2 \cdot \alpha + D)^2 - 16 \cdot \alpha \cdot (S_{eB}/S_f)}} \\ Q_{e2B} &= \frac{4}{\pi} \\ &\cdot \frac{1}{1 + 2 \cdot \alpha - D - \sqrt{(1 - 2 \cdot \alpha + D)^2 - 16 \cdot \alpha \cdot (S_{eB}/S_f)}}. \end{aligned} \tag{26}$$

Note that in (25), there are two unknown parameters, α and S_f. The rest parameters are known quantities. Therefore, from (25), α and S_f can be solved for the real circuit. The results are shown as follows:

$$\alpha_{real} = \frac{S_{eB} \cdot (\frac{4}{Q_2 \cdot |G_{VC}|_A} + \pi^2 \cdot D) - S_{eA} \cdot (\frac{4}{Q_2 \cdot |G_{VC}|_B} + \pi^2 \cdot D)}{2 \cdot \pi^2 \cdot (S_{eB} - S_{eA})} \tag{27}$$

$$S_{f\_real} = \frac{4 \cdot \pi^2 \cdot S_{eA}}{(\frac{4}{Q_2 \cdot |G_{VC}|_A} + \pi^2 \cdot D) \cdot \frac{1}{\alpha} - 2 \cdot \pi^2}. \tag{28}$$

Then, substituting the expressions of α_{real} and Sf_real into (2) and (6) leads to (21) and (22), respectively.

ACKNOWLEDGMENT

The authors would like to thank SIMPLIS Technologies Corporation, USA for providing SIMPLIS simulation tool.

REFERENCES

[1] Monolithic Power Systems, "16V, 12A, Synchronous Step-Down Converter with Adjustable Current Limit, Programmable Frequency," Voltage Tracking MPQ8633A Datasheet, Aug. 2019. [Online]. Available: https://www.monolithicpower.com/en/mpq8633a.html

[2] Richtek Technology Corporation, 3 A, 18 V, 500 kHz, ACOTTM Step-Down Converter RT6214A/B Datasheet, Aug. 2018. [Online]. Available: https://www.richtek.com/assets/product_file/RT6214A = RT6214B/DS6214AB-08.pdf

[3] Texas Instruments, "12-A step-down regulator with integr. Switcher TPS53315 Datasheet, Dec. 2015. [Online]. Available: http://www.ti.com/product/TPS53315

[4] R. W. Erickson and D. Maksimovic, *Fundamentals Power Electron*, Norwell, MA, USA: Kluwer, 2001.

[5] J. Li and F. C. Lee, "New modeling approach and equivalent circuit representation for current-mode control," *IEEE Trans. Power Electron.*, vol. 25, no. 5, pp. 1218–1230, May 2010.

[6] R. Redl and J. Sun, "Ripple-based control of switching regulators—An overview," *IEEE Trans. Power Electron.*, vol. 24, no. 12, pp. 2669–2680, Dec. 2009.

[7] J. Li, F. C. Lee, "Modeling of V^2 current-mode control," *IEEE Trans. Circuits Syst. I*, vol. 57, no. 9, pp. 2552–2563, Sep. 2010.

[8] S. Tian, F. Lee, P. Mattavelli, K. Cheng, and Y. Yan, "Small-signal analysis and optimal design of external ramp for constant on-time V^2 control with multilayer ceramic caps," *IEEE Trans. Power Electron.*, vol. 29, no. 8, pp. 4450–4460, Aug. 2014.

[9] Y. C. Lin, C. J. Chen, D. Chen, and B. Wang, "A ripple-based constant on-time control with virtual inductor current and offset cancellation for DC power converters," *IEEE Trans. Power Electron.*, vol. 27, no. 10, pp. 4301–4310, Oct. 2012.

[10] L. Kong, D. Chen, S. F. Hsiao, C. F. Nien, C. J. Chen, and K. F. Li, "A novel adaptive-ramp ripple-based constant on-time buck converter for stability and transient optimization in wide operation range," *IEEE J. Emerg. Sel. Top. Power Electron.*, vol. 6, no. 3, pp. 1314–1324, Sep. 2018.

[11] Y. Yan, F. C. Lee, and P. Mattavelli, "Unified three-terminal switch model for current mode controls," *IEEE Trans. Power Electron.*, vol. 27, no. 9, pp. 4060–4070, Sep. 2012.

[12] K. Y. Cheng, F. Yu, P. Mattavelli, and F. C. Lee, "Characterization and performance comparison of digital V^2-type constant on-time control for buck converters," in *Proc. IEEE 12th Workshop Control Model. for Power Electron.*, 2010, pp. 1–6.

[13] K. Y. Cheng, F. Yu, F. C. Lee, and P. Mattavelli, "Digital enhanced V^2-type constant on-time control using inductor current ramp estimation for a buck converter with low-ESR capacitors," *IEEE Trans. Power Electron.*, vol. 28, no. 3, pp. 1241–1252, Mar. 2013.

[14] C. J. Chen, D. Chen, C. W. Tseng, C. T. Tseng, Y. W. Chang, and K. C. Wang, "A novel ripple-based constant on-time control with virtual inductor current ripple for buck converter with ceramic output capacitors," in *Proc. IEEE Appl. Power Electron. Conf.*, 2011, pp. 1488–1493.

[15] P. Liu, Y. Yan, P. Mattavelli, and F. C. Lee, "Digital constant on-time V^2 control with hybrid capacitor current ramp compensation," *IEEE Trans. Power Electron.*, vol. 33, no. 10, pp. 8818–8826, Oct. 2018.

[16] Y. Yan, F. C. Lee, S. Tian, and P. H. Liu, "Modeling and design optimization of capacitor current ramp compensated constant on-time V^2 control," *IEEE Trans. Power Electron.*, vol. 33, no. 8, pp. 7288–7296, Aug. 2018.

[17] C. Nien *et al.*, "A novel adaptive quasi-constant on-time current-mode buck converter," *IEEE Trans. Power Electron.*, vol. 32, no. 10, pp. 8124–8133, Oct. 2017.

[18] X. Ming, Y. Xin, T. Li, H. Liang, Z. Li, and B. Zhang, "A constant on-time control with internal active ripple compensation strategy for buck converter with ceramic capacitors," *IEEE Trans. Power Electron.*, vol. 34, no. 9, pp. 9263–9278, Sep. 2019.

[19] J. J. Lu, C. Chen, C. Hong, and C. Tsai, "A novel ripple-coupling constant on-time controlled buck converter ic with highly digital charge-pump based error amplifier," in *Proc. IEEE Appl. Power Electron. Conf. Expo.*, 2019, pp. 1766–1769.
[20] Y. Li, C. Chen, and C. Tsai, "A constant on-time buck converter with analog time-optimized on-time control," *IEEE Trans. Power Electron.*, vol. 35, no. 4, pp. 3754–3765, Apr. 2020
[21] V. Li, Q. Li and F. C. Lee, "Improved V^2 constant on-time control with state-trajectory control," in *Proc. IEEE Appl. Power Electron. Conf. Expo.*, New Orleans, LA, USA, 2020, pp. 3031–3038.
[22] R. D. Middlebrook, "Measurement of loop gain in feedback systems," *Int. J. Electron.*, vol. 38, no. 4, pp. 485–512, 1975.
[23] S. F. Hsiao, D. Chen, C. J. Chen, and H. S. Nien, "A new multiple-frequency small-signal model for high-bandwidth computer v-core regulator applications," *IEEE Trans. Power Electron.*, vol. 31, no. 1, pp. 1185–1192, Jan. 2016.
[24] B. Wang, S. Wang, D. Chen, K. Huang, B. Tai, and E. Tseng, "Practical simulations of control characteristics of a current-mode DC/DC converter," in *Proc. IEEE Power Electron. Spec. Conf.*, 2006, pp. 1–5.
[25] Omicron Lab, Bode 100 datasheet, 2017. [Online]. Available: https://www.omicron-lab.com/fileadmin/assets/Bode_100/Documents/Bode_100_R2_Technical_Data_V1.2.pdf

Brian Wang received the B.S. degree from the Department of Electrical Engineering, National Tsing Hua University, Hsinchu, Taiwan, in 2004, and the M.S. degree from the Graduate Institute of Electronics Engineering, National Taiwan University, Taipei, Taiwan, in 2006.

He was involved in researching dc–dc converters and modeling, analysis, and simulation. From 2006 to 2013, he was an Application Engineer with Richtek Technology Corporation, Taiwan. From 2011 to 2013, he was with uPI Semiconductor Corporation, as a Deputy Manager of the Application Engineer Group. From 2013 to 2016, he was a Manager of PowerEdge Server DC–DC Engineer Group with Dell Technologies, Inc. Since 2016, he has been a Senior Manager of Applications Engineer Group in Monolithic Power Systems, Inc. He is actively involved in power electronics research in the areas of Power IC, control and modeling, computer-aided design, and simulation for power electronics systems.

Dan Chen (Fellow, IEEE) received the B.S.E.E. degree from National Chiao Tung University, Hsinchu, Taiwan, in 1969, and the Ph.D. degree in electrical engineering from Duke University, Durham, NC, USA, in 1975.

From 1975 to 1979, he was with the G.E. Corporate Research Center, Schenectady, NY, USA, where he worked on power electronic applications including electric car and electronic ballast applications. From 1979 to 2003, he was with the Department of Electrical Engineering, Virginia Polytechnic Institute and State University, Blacksburg, VA, USA and was a core Professor with the National Science Foundation's Center for Power Electronic Systems. Since September 2003, he has been a Distinguished Professor with the Department of Electrical Engineering, National Taiwan University, Taiwan. In 1986, he also cofounded Motion Control System, Inc., a company dedicated to brushless dc motor and control, in Dublin, VA, USA, where he served as the Chief Consultant until 2003. He has published numerous papers, held 20 patents, and coedited a book on "*Power Transistors and Their Applications*" (Piscataway, NJ, USA: IEEE press) in 1984. His research interest incudes power conversion systems, power semiconductor device characterization, EMI in switching circuits, and more recently power ICs.

Prof. Chen was recipient of the IEEE Aerospace Society Barry Carlton Award in 1975, the NASA Invention Award in 1986, and the IEEE Power Electronics Society Best Paper Award in 1998.

Ching-Jan Chen (Senior Member, IEEE) received the B.S. and Ph.D. degrees in electrical engineering from National Taiwan University, Taipei, Taiwan, in 2006 and 2011, respectively.

From 2010 to 2011, he was a Visiting Scholar with the Center of Power Electronic Systems (CPES) of Virginia Tech., Blacksburg, VA, USA. From 2011 to 2015, he was a Senior Engineer with IC Research and Development Department, Richtek Technology Corporation, Hsinchu, Taiwan, where his work was focused on new control scheme development and IC design of the voltage regulator controller for CPU power. In February 2015, he became an Assistant Professor with the Department of Electrical Engineering, National Taiwan University (NTU), Taiwan, where he is currently an Associate Professor. His current research interests include modeling and control of dc–dc and ac-dc power converters, power conversion for CPU and mobile devices, and power IC design.

Prof. Chen is the recipient of the Young Researcher Award from the Ministry of Science and Technology, Taiwan, in 2016, and the Outstanding Teaching Award from NTU, and the Research Contribution Award from NTU EECS in 2020. He served as session chair, topic chair, and financial chair in several IEEE conferences and competitions including ECCE, ECCE-Asia, International Future Energy Challenge (IFEC), IFEEC, WiPDA Asia, ITEC-Asia Pacific, and VLSI-DAT. He is Secretary and Vice-Chair of IEEE PELS Taipei Chapter from 2018 to 2020 and received the IEEE PELS Best Chapter Award in 2018.

Sheng-Fu Hsiao was born in Kaohsiung, Taiwan, in 1985. He received the B.S. degree from the National Taipei University of Technology, Taipei, Taiwan, in 2008, the M.S. degree from National Cheng Kung University, Tainan, Taiwan, in 2010, and the Ph.D. degree from National Taiwan University, Taipei, Taiwan, in 2016, all in electrical engineering.

From 2010 to 2016, he was a Senior Engineer in the System Development Department, Richtek Technology Corporation, Hsinchu, Taiwan, where his work focused on system analysis and design of voltage regulator controller for central processor unit and computer power. Since May 2016, he has been a Senior Engineer with the System Development Department, Silergy Corporation, Kaohsiung, Taiwan, where his work focuses on digital power solutions development. His current research interests include modeling and control of converters, power ICs, smart power management ICs, and finite-element analysis for magnetic field.